

# X-Ray surface brightness and gas density fluctuations in the Coma cluster

E. Churazov,<sup>1,2</sup> A. Vikhlinin,<sup>3,2</sup> I. Zhuravleva,<sup>1</sup> A. Schekochihin,<sup>4</sup>  
I. Parrish,<sup>5</sup> R. Sunyaev,<sup>1,2</sup> W. Forman,<sup>3</sup> H. Böhringer,<sup>6</sup> S. Randall<sup>3</sup>

<sup>1</sup> *Max-Planck-Institut für Astrophysik, Karl-Schwarzschild-Strasse 1, 85741 Garching, Germany*

<sup>2</sup> *Space Research Institute (IKI), Profsoyuznaya 84/32, Moscow 117997, Russia*

<sup>3</sup> *Harvard-Smithsonian Center for Astrophysics, 60 Garden St., Cambridge, MA 02138, USA*

<sup>4</sup> *Rudolf Peierls Center for Theoretical Physics, University of Oxford, Oxford, OX13NP, UK*

<sup>5</sup> *Department of Astronomy and Theoretical Astrophysics Center, University of California Berkeley, Berkeley, CA 94720, USA*

<sup>6</sup> *MPI für Extraterrestrische Physik, P.O. Box 1603, 85740 Garching, Germany*

10 April 2012

## ABSTRACT

X-ray surface brightness fluctuations in the core ( $650 \times 650$  kpc) region of the Coma cluster observed with XMM-Newton and Chandra are analyzed using a 2D power spectrum approach. The resulting 2D spectra are converted to 3D power spectra of gas density fluctuations. Our independent analyses of the XMM-Newton and Chandra observations are in excellent agreement and provide the most sensitive measurements of surface brightness and density fluctuations for a hot cluster. We find that the characteristic amplitude of the volume filling density fluctuations relative to the smooth underlying density distribution varies from 7-10% on scales of  $\sim 500$  kpc down to  $\sim 5\%$  at scales  $\sim 30$  kpc. On smaller spatial scales, projection effects smear the density fluctuations by a large factor, precluding strong limits on the fluctuations in 3D. On the largest scales probed (hundreds of kpc), the dominant contributions to the observed fluctuations most likely arise from perturbations of the gravitational potential by the two most massive galaxies in Coma, NGC4874 and NGC4889, and the low entropy gas brought to the cluster by an infalling group. Other plausible sources of X-ray surface brightness fluctuations are discussed, including turbulence, metal abundance variations, and unresolved sources. Despite a variety of possible origins for density fluctuations, the gas in the Coma cluster core is remarkably homogeneous on scales from  $\sim 500$  to  $\sim 30$  kpc.

**Key words:** turbulence, galaxies: clusters: general, galaxies: individual: Coma cluster, galaxies: clusters: intracluster medium, X-rays: galaxies: clusters

## 1 INTRODUCTION

The hot intracluster medium (ICM), which fills the cluster gravitational potential, is the dominant baryonic component of rich galaxy clusters. In a smooth and static gravitational potential, the gas in hydrostatic equilibrium should have a smooth density and temperature distribution aligned with the equipotential surfaces. From X-ray data both the density and temperature radial profiles are routinely measured, and the comparison of mass estimates from hydrostatic equilibrium and lensing suggests overall good agreement (to within

10-20%). However, there are a variety of reasons why the gas properties may be perturbed on a range of spatial scales: perturbation of the gravitational potential, turbulent gas motions, imperfect mixing of the gas with different entropies displaced by gas motions, presence of bubbles filled with relativistic plasma, etc. These perturbations of the ICM properties can be detected in raw observational data as flux (surface brightness) fluctuations, variations of temperature, or variations of the projected velocity field (which can be measured with future high resolution X-ray calorimeters, like ASTRO-H).

Several previous studies have explored fluctuations in galaxy clusters. X-ray surface brightness fluctuations on arc-minute scales, relative to a smooth model, were detected for a sample of clusters using the Einstein Observatory data (Soltan & Fabricant 1990). Projected pressure fluctuations in the Coma cluster, using XMM-Newton observations were studied by Schuecker et al. (2004). Another approach was adopted by Kawahara et al. (2008), where the distribution function of the surface brightness fluctuation was calculated for the A3667 cluster and linked to the 3D density fluctuations.

Here we present an analysis of the X-ray surface brightness fluctuations in the core of the Coma cluster using both Chandra and XMM-Newton observations, calculate the power spectrum of these fluctuations and estimate the amplitudes of the 3D density fluctuations on scales ranging from 30 kpc to 500 kpc. The projected pressure fluctuations have been analyzed by Schuecker et al. (2004) over a limited range of spatial scales. Using X-ray surface brightness instead of pressure allows one to probe smaller spatial scales and greatly simplifies accounting for statistical noise.

In our work the choice of the Coma cluster was motivated by three factors: proximity (thus allowing us to probe small physical scales), presence of a large flat surface brightness X-ray core (simplifying the conversion of 2D power spectra to 3D) and brightness of the cluster. The extension of the analysis to even brighter and closer clusters, in particular, Perseus and M87, is straightforward and will be presented elsewhere.

Throughout the paper the redshift of Coma was assumed to be  $z = 0.023$ , corresponding to an angular diameter distance of 93 Mpc (for  $h = 0.72$ );  $1''$  corresponds to 0.45 kpc.

This paper is organized as follows: in §2 we describe the data-sets used in the analysis. In §3 the relation between 2D and 3D power spectra is explained. The measurements of the density fluctuation power spectrum are presented in §4. The implications of our results are discussed in §5 and §6 contains our conclusions.

## 2 DATA AND INITIAL PROCESSING

For our analysis we used publicly available XMM-Newton and Chandra data.

For Chandra, the following OBSIDs were used: 555, 556, 1086, 1112, 1113, 1114, 9714, 10672. The data were prepared following the procedure described in Vikhlinin et al. (2005). This includes filtering of high background periods, application of the latest calibration corrections to the detected X-ray photons, and determination of the background intensity in each observation. The total exposure of the resulting data set is  $\sim 1.15 \times 10^5$  s.

For XMM-Newton, we used a large set of pointings, covering a field of more than  $1 \times 1$  degrees (although only the most central part of this field was used in the subsequent analysis). The data were prepared by removing background flares using the light curve of the detected events above 10 keV and re-normalizing the “blank fields” background to match the observed count rate in the 11-12 keV

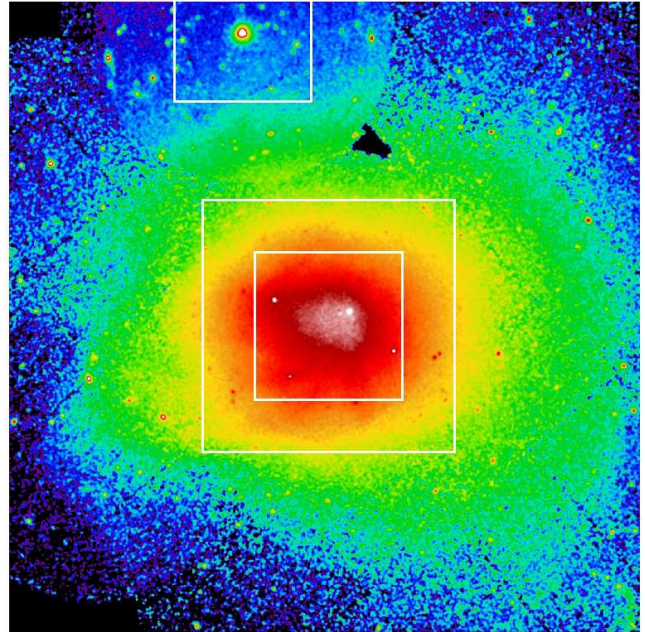


**Figure 1.** XMM mosaic image of Coma ( $1^\circ \times 1^\circ$ , or  $1.6 \times 1.6$  Mpc). Boxes show the regions used for the power spectrum calculation: central  $14' \times 14'$  box - Chandra field; larger  $24' \times 24'$  box - XMM-Newton field. The smallest  $13' \times 13'$  box near the top of the mosaic, which contains the X-ray bright Seyfert galaxy X-Comae, was used to determine the shape of the power spectrum produced by point sources in XMM-Newton images.

band. In the subsequent analysis we used the data from the EPIC/MOS (European Photon Imaging Camera/Metal Oxide Semi-conductor) detector. The total exposure of all used observations is 880 ksec, covering a much larger area than the Chandra observations (not only the cluster core but also the outskirts of the cluster).

The images in the 0.5-2.5 and 0.5-4 keV bands were generated for XMM-Newton and Chandra respectively, along with the exposure and background maps, which were used for subsequent analysis.

The background-subtracted, exposure-corrected XMM-Newton image ( $1^\circ \times 1^\circ$ , or  $1.6 \times 1.6$  Mpc) is shown in Fig.1. For the subsequent analysis of XMM-Newton data only the central  $24' \times 24'$  part of the image was used (roughly corresponding to the flat surface brightness cluster core). For Chandra we also excluded edges of the image with low exposure, keeping only the central  $14' \times 14'$  region.

An azimuthally averaged X-ray surface brightness profile  $I(R)$  is shown in Fig.2. The observed distribution can be reasonably well described by a simple  $\beta$ -model (Cavaliere & Fusco-Femiano 1978) with core radius  $r_c = 9'$  (or  $\sim 245$  kpc) and  $\beta = 0.6$

$$I(R) = \frac{I_0}{\left[1 + \left(\frac{R}{r_c}\right)^2\right]^{3\beta - 0.5}}, \quad (1)$$

where  $R$  is the projected distance from the cluster center and  $I_0$  is the surface brightness at the center. In §4.5 we use this model (and a more complicated one) to remove the

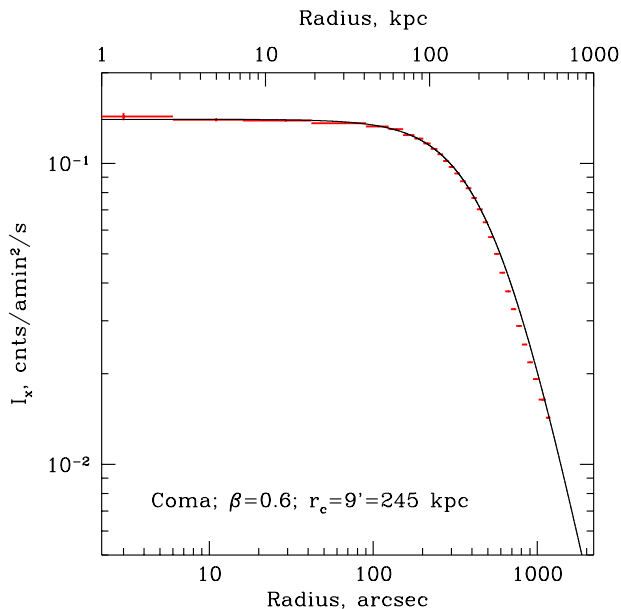


**Figure 2.** Radial X-ray surface brightness profile (XMM-Newton) of the Coma cluster. The solid line shows the surface brightness for a  $\beta$ -model with core radius  $r_c = 9'$  (or  $\sim 245$  kpc) and  $\beta = 0.6$ .

global cluster emission. As discussed in §5.1 the results of our analysis are only weakly sensitive to the particular choice of the  $\beta$ -model. Partly this is because our analysis is applied to the core region of the Coma cluster.

### 3 3D TO 2D PROJECTION

We assume that the density distribution in the cluster is described by a simple decomposition into undisturbed and fluctuating components

$$n(x, y, z) = n_0(x, y, z) [1 + \delta(x, y, z)], \quad (2)$$

where  $n_0(x, y, z)$  is the undisturbed density distribution (e.g. standard spherically symmetric  $\beta$ -model<sup>1</sup> shown in Fig.2 and the dimensionless quantity  $\delta(x, y, z) = \frac{\delta n}{n_0} \ll 1$  describes the fluctuating part. For ICM temperatures above  $\sim 3$  keV, the emissivity of plasma in the soft band, which dominates the flux detected by XMM-Newton and Chandra, mainly depends on the square of the electron density and is only weakly sensitive to the temperature<sup>2</sup>. Accordingly the

<sup>1</sup> One can imagine more complicated models, e.g. ellipsoidal  $\beta$ -model or a model with more sophisticated radial density profiles. In §5 we argue that the freedom in choosing the undisturbed model mostly affects the power spectra at large scale.

<sup>2</sup> The impact of possible abundance variations is briefly discussed in §5.6

volume emissivity  $\varepsilon$  can be written as

$$\varepsilon(x, y, z) = Cn^2(x, y, z) \approx Cn_0^2(x, y, z) [1 + 2\delta(x, y, z)], \quad (3)$$

neglecting terms of order  $\delta^2$  and  $C$  is the coefficient relating the square of the density and the emissivity. Since we are interested in fluctuations, relative to the average surface brightness profile, for the subsequent analysis we set  $C = 1$ . We further assume that  $\delta(x, y, z)$  is a homogeneous and isotropic random field, characterized by the power spectrum  $P_{3D}$ :

$$P_{3D}(k_x, k_y, k_z) = \left| \int \delta(x, y, z) e^{-i2\pi(xk_x + yk_y + zk_z)} dx dy dz \right|^2. \quad (4)$$

By isotropy assumption,  $P_{3D}(k_x, k_y, k_z) = P_{3D}(|k|)$ , where  $k = \sqrt{k_x^2 + k_y^2 + k_z^2}$ .

The observed image  $I(x, y)$  is the integral of the emissivity along the line of sight:

$$I(x, y) = \int \varepsilon(x, y, z) dz = \quad (5)$$

$$\int n_0^2(x, y, z) dz + 2 \int n_0^2(x, y, z) \delta(x, y, z) dz = I_0(x, y) + 2 \int n_0^2(x, y, z) \delta(x, y, z) dz,$$

where  $I_0(x, y)$  is the undisturbed surface brightness. Dividing the observed image by  $I_0(x, y)$  yields the normalized image  $J(x, y)$

$$J(x, y) = 1 + 2 \frac{\int n_0^2(x, y, z) \delta(x, y, z) dz}{\int n_0^2(x, y, z) dz}. \quad (6)$$

The 2D power spectrum of  $J(x, y)$

$$P_{2D}(k_x, k_y) = \left| \int J(x, y) e^{-i2\pi(xk_x + yk_y)} dx dy \right|^2 \quad (7)$$

can be obtained directly from observational data. By isotropy,  $P_{2D} = P_{2D}(k_{xy})$ , where  $k_{xy} = \sqrt{k_x^2 + k_y^2}$ . The expression (6) contains the following function of  $x, y$  and  $z$  under the integral

$$\eta(x, y, z) = \frac{n_0^2(x, y, z)}{\int n_0^2(x, y, z') dz'} = \frac{n_0^2(x, y, z)}{I_0(x, y)}. \quad (8)$$

For the range of projected distances we consider, the weak dependence of  $\eta(x, y, z)$  on  $x$  and  $y$  can be neglected (the changes in  $\eta(x, y, z)$  are at most factor of 2 across the whole image  $24' \times 24'$  for the adopted  $\beta$ -model). Thus  $\eta(x, y, z) \approx \eta(z)$  and the  $P_{2D}$  spectrum can be linked to the  $P_{3D}$  of  $\delta(x, y, z)$  as follows (Peacock 1999, see also Zhuravleva et al. 2011)

$$P_{2D}(k_{xy}) = 4 \int P_{3D}(\sqrt{k_{xy}^2 + k_z^2}) |W(k_z)|^2 dk_z, \quad (9)$$

where  $|W(k_z)|^2$  is the 1D power spectrum of the normalized emissivity distribution along the line of sight.

$$W(k_z) = \int \eta(z) e^{-i2\pi z k_z} dz. \quad (10)$$

Note that the properties of the emission measure distribution along the line of sight determine the characteristic

wavenumber  $k_{z,cutoff}$  above which  $|W(k_z)|^2$  falls off towards larger  $k$ . For  $k \gg k_{z,cutoff}$  the expression (9) simplifies to

$$P_{2D}(k) \approx 4P_{3D}(k) \int |W(k_z)|^2 dk_z, \quad (11)$$

i.e., the 2D power spectrum of the surface brightness fluctuations is essentially equal to the 3D power spectrum of the density fluctuations apart from the normalization constant  $4 \int |W(k_z)|^2 dk_z$ , which is easily measured for a cluster. In principle  $\int |W(k_z)|^2 dk_z$  depends on  $x$  and  $y$  and so is different for different lines of sight, but as we show in Fig.5, for the central region of Coma this difference can be neglected.

For practical reasons it is easier to use the characteristic amplitude of the fluctuations, rather than the power spectrum. The amplitudes corresponding to the 3D and 2D spectra are defined as

$$A_{3D}(k) = \sqrt{P_{3D}(k)4\pi k^3}, \quad (12)$$

$$A_{2D}(k) = \sqrt{P_{2D}(k)2\pi k^2} \quad (13)$$

To illustrate the above relations for the case of Coma, we set the density distribution eq.(3) to the  $\beta$ -model with  $\beta = 0.6$  and core radius  $r_c = 245$  kpc corresponding to the azimuthally averaged Coma surface brightness profile, shown in Fig.2:

$$n_0(r) \propto \left(1 + \frac{r^2}{r_c^2}\right)^{-\frac{3}{2}\beta} \quad (14)$$

and calculated the power spectra of the line-of-sight emissivity distribution at several projected radii. We further parametrize the 3D power spectrum of density fluctuations with a simple cored power law

$$P_{3D}(k) = \frac{B}{\left(1 + \frac{k^2}{k_m^2}\right)^{\alpha/2}}, \quad (15)$$

where  $\alpha$  is the slope of the power spectrum at large  $k$ , where  $k_m$  is the characteristic wavenumber below which the 3D spectrum is flat and  $B$  is the normalization constant. This choice of the power spectrum parametrization is rather arbitrary. It is used only to compare the exact calculation of  $P_{2D}(k)$  using eq.(9) with the approximate formula eq.(11).

Using eq. (15) and the power spectrum  $|W(k_z)|^2$ , the power spectrum of the surface brightness fluctuations can be easily calculated via eq. (9). The resulting characteristic amplitudes  $A_{3D}$  and  $A_{2D}$  for different values of  $k_m$ ,  $\alpha$  and different lines of sight (projected distances) are shown in Figs. 3, 4 and 5 respectively.

In each of these images the dotted lines show the ratio of the 2D and 3D amplitudes, calculated using the exact relation (9) divided by the ratio evaluated using the simplified relation (11), which corresponds to the case of small scale perturbations. Clearly, independently of the shape of the power spectrum (Fig.3 and Fig.4) or projected distance (Fig.5) the simplified relation (11) provides an excellent approximation of the relation between 2D and 3D spectra (unless the power law spectrum extends to very low  $k$ , corresponding to scales of a few Mpc). Furthermore for a given

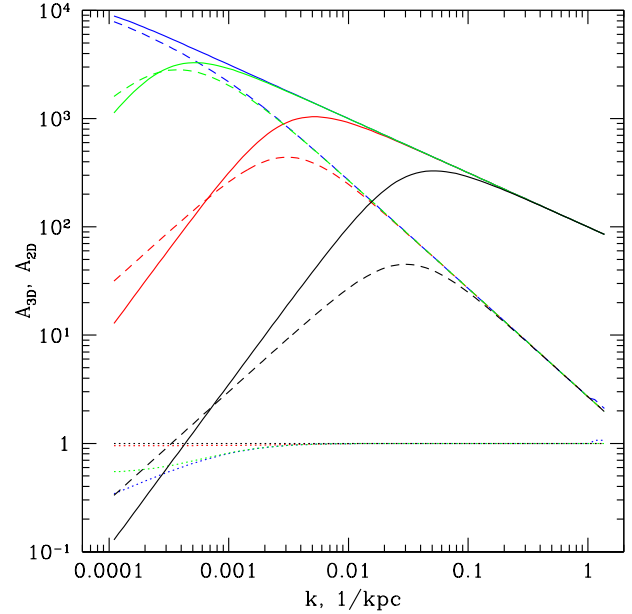


**Figure 3.** 3D and 2D amplitudes as a function of  $k$  for a model power spectrum and for a  $\beta$ -model cluster with  $\beta = 0.6$  and  $r_c = 245$  kpc. A cored power law model is used for the 3D power spectrum, according to eq.(15). Different colors correspond to different break wavenumber (in  $\text{kpc}^{-1}$ ) in the 3D power spectrum:  $k_m = 3 \cdot 10^{-5}$  (blue),  $3 \cdot 10^{-4}$  (green),  $3 \cdot 10^{-3}$  (red),  $3 \cdot 10^{-2}$  (black). Projection (see eq.(9)) is done along the line-of-sight going through the Coma center. Solid curves correspond to  $A_{3D}$ , dashed – to  $A_{2D}$ , dotted – to the ratio of  $A_{2D}$  to the prediction of the simplified expression (11). All dotted curves are very close to unity at  $k \geq 10^{-3} \text{ kpc}^{-1}$ , indicating that expression (11) can be used to relate 3D and 2D amplitudes for  $k \geq 10^{-3} \text{ kpc}^{-1}$ . In this plot, the factor 4 appearing in eq. (9) is omitted.

3D spectrum, the expected 2D spectra, measured at different projected distances from the Coma cluster, differ only in amplitude, and this difference is less than a factor of 2 (provided that the projected distance is less than  $\sim 600$  kpc).

#### 4 MEASURING THE 3D POWER SPECTRUM OF DENSITY FLUCTUATIONS

Our goal is to obtain 3D power spectra of the density fluctuations. Our general strategy is as follows. We start with the analysis of the 2D power spectra of raw images and evaluate the contribution of the Poisson noise and point sources. Then we pick a smooth model as a representation of the undisturbed cluster density distribution, predict the corresponding surface brightness distribution and calculate 2D fluctuations relative to this model. The resulting 2D power spectra are corrected for the telescope Point Spread Function (PSF) effects. We then convert 2D power spectra to 3D spectra using eq.(11) and recast the results in terms of

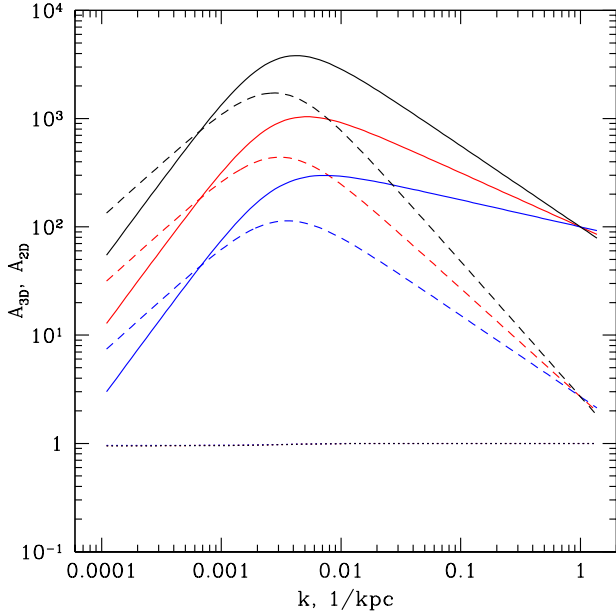


**Figure 4.** 3D (solid) and 2D (dashed) amplitudes as a function of  $k$  for a model power spectrum. Different slopes of the 3D power spectrum  $\alpha = 3.5, 4, 4.5$  are shown with blue, red and black colors respectively.  $k_m = 3 \cdot 10^{-3} \text{ kpc}^{-1}$  is the same for all plots. The dotted line shows the ratio of  $A_{2D}$  to the prediction of the simplified expression (11).

3D amplitudes of density fluctuations relative to the smooth underlying 3D model.

#### 4.1 2D power spectrum evaluation

The method used to evaluate low resolution power spectra of the surface brightness fluctuations is described in Arévalo et al. 2011 (see also Ossenkopf, Krips, & Stutzki 2008). Briefly one convolves the image with a set of Mexican-Hat filters (with different spatial scales)  $F(x) = \left[1 - \frac{x^2}{\sigma^2}\right] e^{-\frac{x^2}{2\sigma^2}}$ , where  $\sigma$  is the characteristic spatial scale<sup>3</sup>, and relates the variance of the resulting image to the power at a given scale. The presence of a non-uniform exposure map or gaps in the data (e.g. excised regions around bright point sources) is accounted for by representing the Mexican Hat filter as a difference between two Gaussians with only slightly different width. For each spatial scale  $\sigma$ , the following simple steps are performed (see Arévalo et al. 2011 for a detailed description):

(i) the observed image  $I$  and the exposure map  $E$  are smoothed with two Gaussians  $G$  having different smooth-

<sup>3</sup> Mexican-Hat filter has a positive core and negative wings, and preferentially selects perturbations with a given scale.

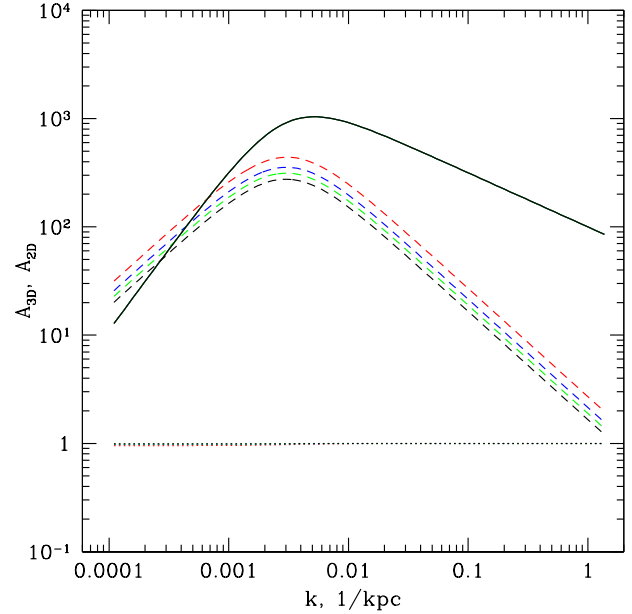


**Figure 5.** 3D (solid) and 2D (dashed) amplitudes as a function of  $k$  for a model power spectrum. The 3D power spectrum has  $k_m = 3 \cdot 10^{-3} \text{ kpc}^{-1}$  and  $\alpha = 4$ . The 2D amplitude is calculated for different projected distances  $R = 0, 300, 435, 600 \text{ kpc}$  (red, blue, green, black respectively). The dotted line shows the ratio of  $A_{2D}$  to the prediction of the simplified expression (11).

ing lengths  $\sigma_1 = \sigma/\sqrt{1+\epsilon}$  and  $\sigma_2 = \sigma\sqrt{1+\epsilon}$ , where  $\epsilon \ll 1$  is a dimensionless number;

(ii) smoothed images are divided by smoothed exposure maps and regions with low (unsmoothed) exposure are masked out;

(iii) the difference of the two images is calculated, this difference image is dominated by fluctuations at scales  $\sim \sigma$ ;

(iv) the variance of the resulting image is calculated and re-cast into an estimate of the power, using a normalization coefficient that depends on  $\epsilon$ .

Thus the variance is calculated for an image

$$I_\sigma = E \times \left( \frac{G_{\sigma_1} \circ I_{raw}}{G_{\sigma_1} \circ E} - \frac{G_{\sigma_2} \circ I_{raw}}{G_{\sigma_2} \circ E} \right), \quad (16)$$

where  $E = E(x, y)$  is the exposure map,  $I_{raw} = I(x, y)$  is the raw image in counts and  $G_\sigma \circ I$  denotes a convolution of an image  $I$  with a Gaussian. The final expression for the power at a given spatial scale (or given wavenumber) is then

$$P_{2D}(k) = \frac{1}{\epsilon^2 \pi k^2} \frac{\sum I_\sigma^2}{\sum E^2}, \quad (17)$$

where summation is over the image pixels (see appendix 1 in Arévalo et al. 2011). The resulting 2D power spectrum for the XMM-Newton image of Coma is plotted in Fig.6 (dashed line). Effectively the power spectrum shown in Fig.6 is a convolution of the true underlying power spectrum with a broad ( $\Delta k \sim k$ ) filter in  $k$  space. Therefore individual measurements of the power are not independent,

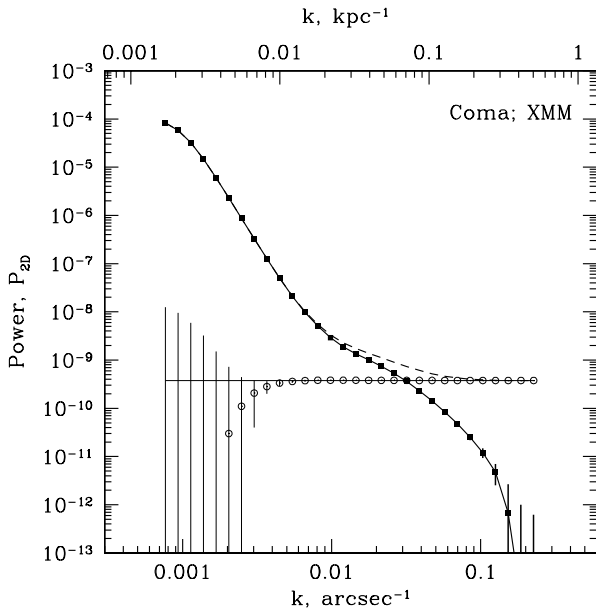


**Figure 6.** Raw power spectrum  $P_{2D}(k)$  (dashed line), eq.(17), of the XMM-Newton field with sources and Poisson noise. The Poisson noise level, estimated using eq.(18), is shown with the thin horizontal line. The Poisson noise evaluated by adding extra Poisson noise to the images (see §4.2) is shown with circles. The Poisson-subtracted power spectrum is shown with the solid line and black squares. The errors shown are due to Poisson noise only and do not account for the stochastic nature of the signal itself.

unlike components of the conventional Fourier transform in a rectangular region. However the procedure adopted here has a clear advantage compared to the conventional Fourier transform, since most of the problems caused by non-periodicity of the data-set and the presence of the gaps in data are automatically corrected for (Arévalo et al. 2011; Ossenkopf, Krips, & Stutzki 2008).

For XMM-Newton and Chandra observations, we decided to use images without instrumental and cosmic background subtraction. Inclusion of the background does not significantly affect the results, but in the case of XMM-Newton it would add some high frequency noise due to weak compact sources, which were not eliminated completely in the blank-field data-sets.

#### 4.2 Poisson noise

The Poisson noise contribution can be easily estimated for the raw images. We expect a white noise (flat) power spectrum\* for this component with the power:

$$P_{Poisson} = \frac{\sum I_{raw}}{\sum E^2}, \quad (18)$$

where summation is over the image pixels. The result of this calculation is shown in Fig.6 with the solid horizontal line.

Very small deviations from this simple estimate are possible due to non-trivial behavior of the filter at the edges of the image or near the data gaps (partly due to the coarse representation of the Mexican Hat filter on a grid for the highest frequency bins). To take care of these possible deviations we made 100 realizations of fake raw images by adding extra Poisson noise to each pixel with the mean value set by the actual number of counts in the pixel. The whole procedure of evaluating the power spectrum is then repeated and the mean of the resulting power spectra is calculated. Effectively this mean power spectrum has an extra Poisson noise component (compared to the original image) with all properties similar to the Poisson noise in the original image. Therefore the difference between the mean power spectrum and the original power spectrum provides an estimate of the Poisson noise contribution, which includes all possible effects of the filter implementation.

As expected, the derived noise spectrum has an essentially flat spectrum. The same procedure allows us to evaluate uncertainties caused by the presence of Poisson noise in the power spectrum. The estimated level of the Poisson noise and corresponding uncertainties (in evaluating the Poisson noise) are shown in Fig.6 as black circles with error bars.

The power spectrum with the Poisson noise contribution subtracted is shown with the solid curve. The errorbars shown are due to the Poisson noise only.

#### 4.3 Point sources

The Poisson-noise-subtracted power spectrum (solid line in Fig.6) changes slope at  $k \sim 0.01 \text{ arcsec}^{-1}$ . At larger  $k$ , the spectrum flattens. This flattening is at least partly caused by the presence of compact sources in the image. Indeed, ignoring the blurring of an image by the PSF of the telescope, the presence of compact sources (i.e.  $f_{src} \delta(x - x_{src}, y - y_{src})$ , where  $\delta$  is the Dirac delta-function at the position of a source with flux  $f_{src}$ ), randomly scattered across the image, produces a flat power spectrum over the entire range of wavenumbers. Accounting for the telescope PSF, having Gaussian width  $\sigma$ , the expected contribution of point sources has the shape of the PSF power spectrum, which is flat at  $k \ll 1/\sigma$  and falls off at larger wavenumbers.

As a first step towards removing the contribution of compact sources we excised a  $15''$  circle (radius) from the images around each bright, individually detected source. The exposure map has been modified accordingly. The power spectra calculated from the images without bright sources are shown in Fig.7 with the blue curves. Clearly, much of the high-frequency part of the power spectrum goes away once bright sources are excluded. For comparison, the raw power spectrum is shown with black symbols.

To confirm still further that much of the detected higher-frequency power is attributable to the point sources, we computed the power spectrum for images containing a large number of bright compact sources.

For Chandra, we used one of the long observations of the Lockman Hole with ACIS-I and used a  $14' \times 14'$  patch of the image. The power spectrum obtained from this field after correction for Poisson noise is shown in Fig.8. We also

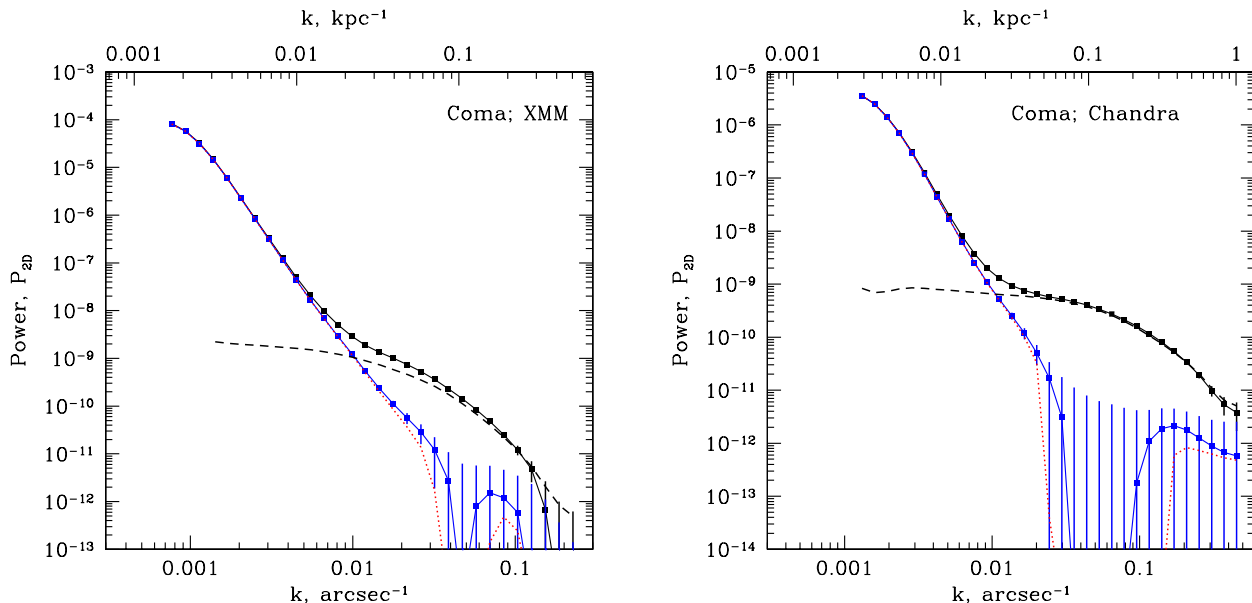


**Figure 7.** Power spectra of raw images with point sources (black solid) and with  $15''$  circles around point sources excluded (blue solid) for XMM-Newton field (left) and Chandra field (right). Black dashed lines show the expected shape of a power spectrum associated with point sources, taken from the X-Comae and Lockman fields for XMM-Newton and Chandra respectively (see §4.3). Dotted red lines show the effect of subtracting an extra component, associated with weak point sources, which are too faint to be detected individually in the images. The normalization of this subtracted component is estimated to be  $\approx 3\%$  of the power spectrum due to bright detected sources (see §4.3).

plot the same power spectrum in Fig.7 with a dashed line, changing only the normalization of the spectrum. Clearly the shape of the shoulder in the power spectrum calculated for a raw image of Coma (including compact sources) is consistent with the power spectrum observed in the Lockman Hole data.

For XMM-Newton, we used a patch of the image to the NE from the Coma center (Fig.1). This patch contains the X-ray bright Seyfert galaxy X-Comae and a number of weaker sources. The power spectrum calculated for this image is shown in Fig.9. Similarly to Chandra, this power spectrum has a shape consistent with the shape of the shoulder obtained from the raw image of Coma (including compact sources) as shown in Fig.7. The properties of the PSF vary across the telescope field of view. We used a field close to the Galactic Plane (OBSID: 0605580901), containing many compact sources across the field, to verify that the shape of the PSF power spectrum obtained from the X-Comae field is not too strongly dominated by the X-Comae itself, which was observed close to the center of the XMM-Newton field of view. The resulting power spectrum of the Galactic Plane image is consistent with the X-Comae patch over the interesting range of wavenumbers.

An additional question arises in connection with XMM-Newton data: is a  $15''$  circle around a source large enough to sufficiently suppress the contribution to the Power Spectrum of the PSF wings? To address this question, we repeated

the calculation of the power spectrum for the patch near X-Comae, excluding  $15''$  and  $30''$  circles around each source (see Fig.10). The corresponding power spectra are shown in Fig.9. From the comparison of these spectra with the full power spectrum of the X-Comae patch, it is clear that removing  $15''$  circles suppresses the high frequency noise by a factor of order 300, while  $30''$  circles suppress the signal<sup>4</sup> by a factor of a few 1000. For our purposes, the suppression factor of more than a 100 is enough and we fixed the size of the excised region around each point source to  $15''$  (radius).

Apart from the bright detected sources there must be faint compact objects that we failed to detect. Their collective contribution can be estimated assuming that we know the LogN-LogS and limiting fluxes. To this end we calculated fluxes of our detected sources using a  $15''$  circle as a source region and a twice larger circle as a background region for each source (for Chandra the size of the region is probably larger than necessary, but it is not very important for the present study). The LogN-LogS curves for both instruments are shown in Fig.11 (note, that the XMM field is larger than the Chandra field). The curves can be reasonably well approximated by the law  $N \propto F^{-1}$ . Assuming that

<sup>4</sup> Note that there is significant contribution of Coma cluster diffuse emission to the field. For this reason the signal does not go to zero even for the larger size of the excised regions.

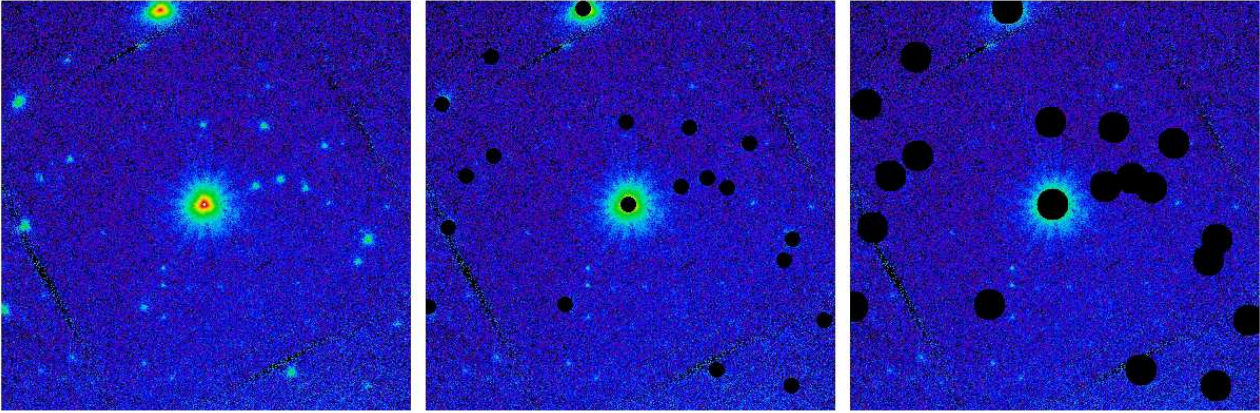


**Figure 10.** Patch of the XMM-Newton image ( $13' \times 13'$ ) near the bright Seyfert galaxy X Comae. In the middle and right panels the circles with radius  $15''$  and  $30''$  are excised around bright sources.

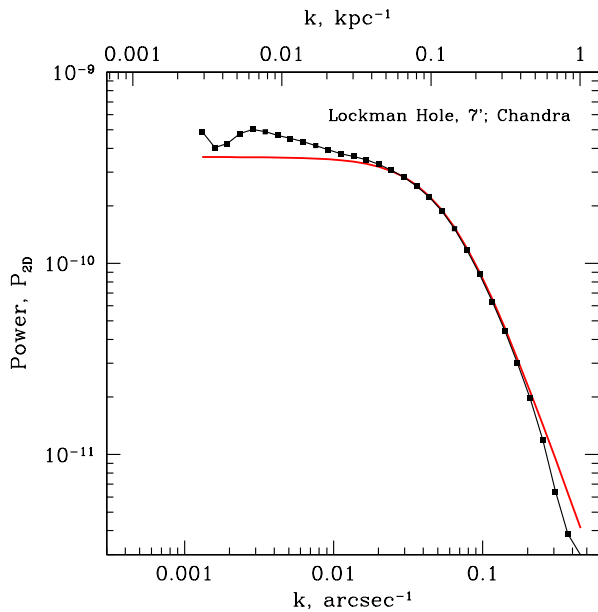


**Figure 8.** Power spectrum (black) of the Chandra Lockman Hole image. The red curve shows the crude approximation of the power spectrum of the Lockman Hole field by a simple model (see §4.4 and eq.22)

the same slope continues at lower fluxes we can estimate the contribution of faint point sources to the power spectrum:

$$P_{faint} \propto \int_0^{F_1} \frac{dN}{dF} F^2 dF \propto F_1, \quad (19)$$

where  $F_1$  is the minimal flux of the detected source. For XMM  $F_1 \sim 100$  counts. It is convenient to relate  $P_{faint}$  to the combined contribution of bright detected sources:

$$P_{bright} \propto \int_{F_1}^{F_2} \frac{dN}{dF} F^2 dF \propto F_2, \quad (20)$$

provided  $F_2 \gg F_1$ , where  $F_2$  is the flux of the brightest detected source (assuming that the same slope of LogN-LogS is applicable to the entire range from  $F_1$  to  $F_2$ ). For XMM-Newton  $F_2 \sim 3000$  counts. Thus the contribution of unresolved sources can be estimated to be at the level of  $\frac{F_1}{F_2} \sim 0.03$  relative to the known contribution of bright sources to the power spectrum. We used the difference between the power spectra with and without sources to calculate the power spectrum associated with bright sources  $P_{bright} = P_{withsrc} - P_{nosrc}$  and multiplied  $P_{bright}$  by 0.03. The subtraction of this extra component modifies the high frequency side of the power spectrum (see Fig.7), but the magnitude of the modification does not exceed the uncertainties in the power spectrum, associated with pure Poisson noise. Given the uncertainties in estimating this component and taking into account that it is mostly important in the range of wavenumbers where Poisson noise dominates the signal, in the analysis below we neglect this component.

#### 4.4 Correction of the Coma power spectrum for PSF

Analysis of the images containing bright point sources can also be used to evaluate the effective power spectrum of the telescope PSF. Indeed, the convolution of the true sky image with the telescope PSF is equivalent to the multiplication of the true sky power spectrum by the PSF power spectrum. Note that the PSF shape may vary across the instrument Field of View (FoV), so one needs to perform the analysis separately for different parts of the FoV, or use some effective PSF (e.g. FoV averaged). We decided to follow the second approach and simply used the observed power spectra for the Lockman Hole (Chandra) and X-Comae region (XMM-Newton) as the PSF power spectrum (see Fig.8,9) approximated with the following simple analytic models:

$$P_{PSF,Chandra} = \frac{1}{\left[1 + \left(\frac{k}{0.06}\right)^2\right]^{1.1}} \quad (21)$$

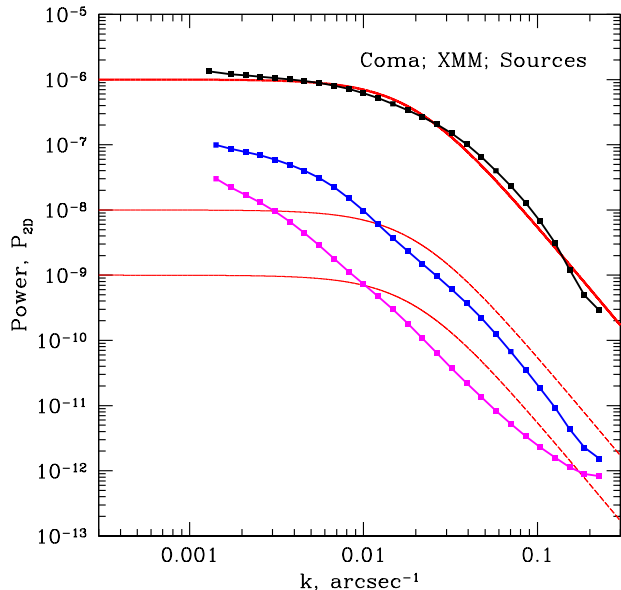


**Figure 9.** Power spectra for a patch near X Comae. Black curve - the power spectrum from the image with sources (see Fig.10, left panel). Blue - power spectrum when 15'' circles (radius) around bright sources are excluded (see Fig.10, middle panel). Magenta - power spectrum when 30'' circles excluded (see Fig.10, right panel). Thick red curve shows a simple approximation of the PSF power spectrum (see §4.4 and eq.22). Lower red curves show the same spectrum scaled down by a factor of 100 and 1000. From this plot one can conclude that excising 15'' circle around a bright source reduces the contribution of the source to the power spectrum by a factor of  $\sim 300$  or more (see §4.3).

$$P_{PSF,XMM} = \frac{1}{\left[1 + \left(\frac{k}{0.02}\right)^2\right]^{1.6}}, \quad (22)$$

for Chandra and XMM respectively, where the wavenumber  $k$  is in units of  $\text{arcsec}^{-1}$ . The correction for PSF blurring is done by dividing the power spectrum of the raw image by the power spectrum of the PSF.

#### 4.5 Removing the global surface brightness profile

As discussed in §3 it is convenient to divide the surface brightness of the raw image by the predictions of a simple model, describing the global properties of Coma. The divided image can then be interpreted as fluctuations of the surface brightness relative to the undisturbed image. To this end we experiment with using a simple symmetric  $\beta$ -model (see §2) as an approximation of the cluster global surface brightness distribution or a slightly more sophisticated two-dimensional  $\beta$ -model, which allows for two different core radii and rotation. For illustration the image divided by the symmetric  $\beta$ -model is shown in the bottom-right corner of Fig.12. In practice both symmetric and two-dimensional

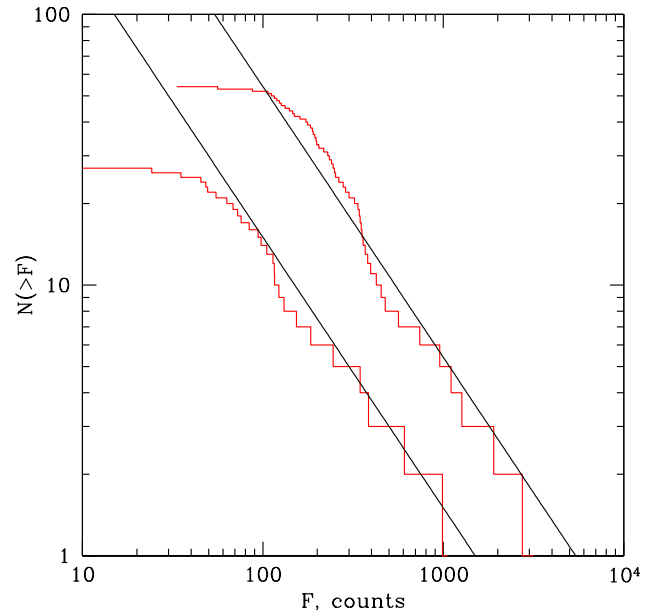


**Figure 11.** LogN-LogS for detected sources in XMM and Chandra fields (upper and lower red histograms, respectively). The flux (in counts) for each source was calculated in 15'' circle, using 30'' for the background. Black solid lines show the  $F^{-1}$  law. Assuming that the same law continues to lower fluxes, one can estimate the contribution of faint (undetected) sources to the power spectrum (see §4.3).

$\beta$ -models yield similar power spectra, except at the lowest wavenumbers (see §5.1).

The resulting 2D power spectra (normalized by the symmetric  $\beta$ -model, with point sources excised, Poisson noise level subtracted) are shown in Fig.13. In this plot the 2D power spectrum was converted into the characteristic amplitude of the surface brightness fluctuations relative to the smooth model. The measured amplitude of perturbations of the surface brightness (before the PSF correction) varies from  $\sim 10\%$  at scales of  $\sim 500$  kpc down to less than 1% at scales of  $\sim 30$  kpc.

#### 4.6 Converting to 3D and the amplitude of density fluctuations

The final step of the analysis is the conversion of the 2D surface brightness fluctuations (relative to the underlying undisturbed image) to the 3D density fluctuation power spectrum or amplitude of the 3D density fluctuations. As described in §3, the easiest way of obtaining the 3D power spectrum is to use the approximate relation between the 3D and 2D spectra according to eq.(11), which for model power spectra works well at wavenumbers of order  $10^{-3} \text{ kpc}^{-1}$  and larger. It is also convenient to convert the final power spectrum to the amplitude of the density perturbations using eq.(12). The final results of this analysis are shown in Fig.14.

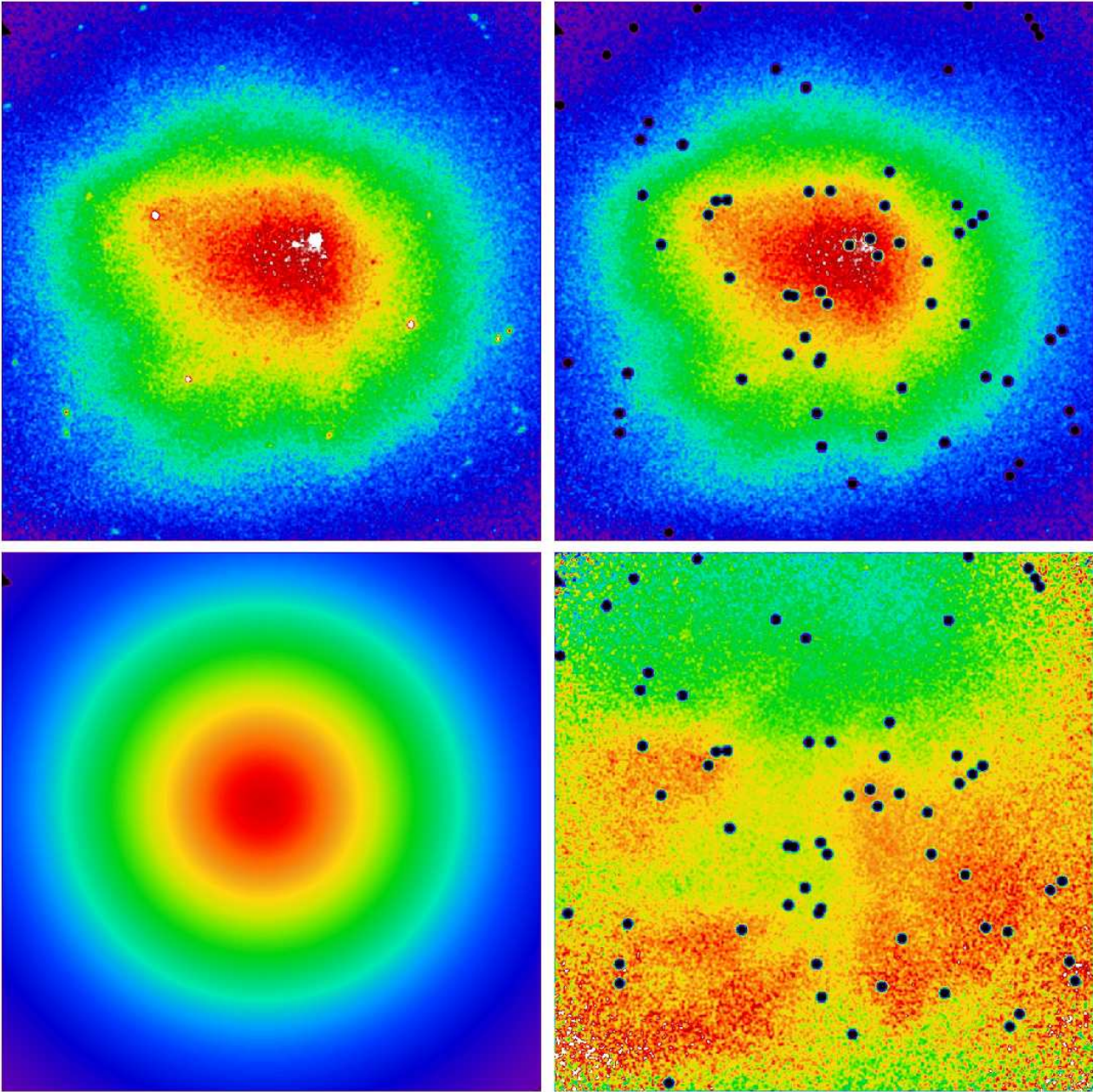


**Figure 12.** Top-left: raw XMM-Newton image; Top-Right: image with  $15''$  circles around bright point sources removed; Bottom-Left: surface brightness for a  $\beta$ -model with  $\beta = 0.6$  and core radius  $r_c = 245$  kpc; Bottom-Right: XMM-Newton image divided by the  $\beta$ -model. All images are  $24' \times 24'$  (or  $648 \times 648$  kpc). Images are slightly smoothed with a Gaussian filter.

This 3D amplitude characterizes typical variations of the density relative to the unperturbed value (i.e.  $\frac{\delta\rho}{\rho} \equiv A_{3D}$ ) as a function of the spatial scale. The amplitude varies from  $\sim 10\%$  at scales of a few 100 kpc down to  $\sim 5\%$  at scale of a few tens of kpc. At even smaller scales, pure statistical errors due to Poisson noise increase dramatically precluding tight constraints on the amplitude of the fluctuations.

## 5 DISCUSSION

The main conclusion one can draw from Fig.14 is that there are significant variations of the density fluctuations of the ICM on spatial scales ranging from  $\sim 500$  kpc down to  $\sim 30$  kpc at the level of 5 to 10%. These fluctuations are relatively small over the entire range of wavenumbers where the existing data have sufficient statistics to make accurate measurements. Large-scale fluctuations are directly visible in the images divided by a suitable smooth model as excesses or dips in the surface brightness (Fig.12), although their ap-

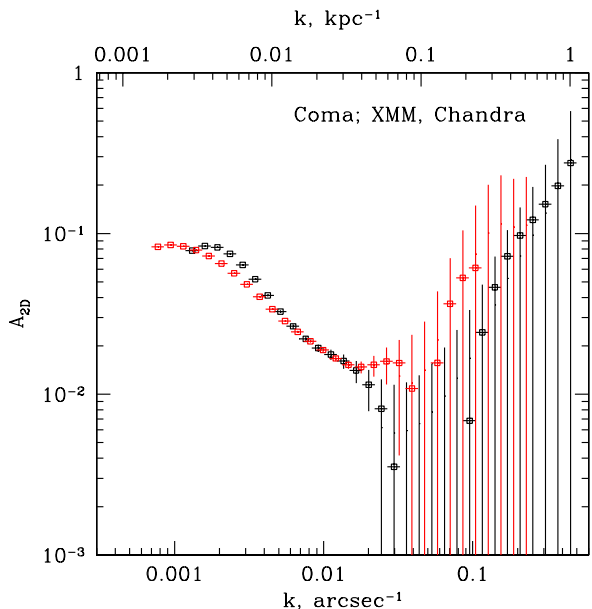


**Figure 13.** 2D amplitude of X-ray brightness fluctuations (relative to the underlying  $\beta$ -model) as a function of the wavenumber. Black - Chandra, red - XMM-Newton. The uncertainties shown are due to Poisson noise only and do not account for the stochastic nature of density fluctuations. The PSF correction (see §4.4) is taken into account.

pearance does vary depending on the type of the smooth model. Small-scale perturbations are in the regime dominated by the Poisson noise and they are revealed only in a statistical sense and not individually visible in the image.

There are several plausible physical mechanisms which can lead to the observed emissivity/density fluctuations. Among them are the following possibilities:

- too simplistic model of the unperturbed gas density distribution;
- perturbations of the gravitational potential on top of a smooth global potential of the cluster;
- entropy fluctuations caused by infalling low entropy gas or by advection of gas from one radius to another by gas motions;
- variations of gas density and/or pressure associated with gas motion and sound waves;
- metallicity variations;
- presence of non-thermal and spatially variable components (bubbles of relativistic plasma and magnetic fields).

We now briefly discuss these possibilities.

### 5.1 Simplistic smooth model

One of the principal uncertainties in calculating deviations of the surface brightness or density fluctuations lies in specifying the smooth underlying model. Our experiments with a

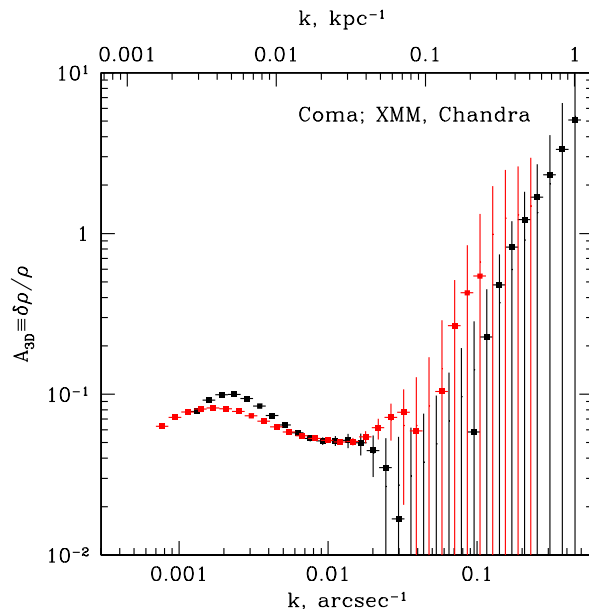


**Figure 14.** 3D amplitude of density fluctuations (relative to the underlying  $\beta$ -model) as a function of the wavenumber. Black - Chandra, red - XMM-Newton. The uncertainties shown are due to Poisson noise only and do not account for the stochastic nature of density fluctuations. The effect of the PSF has been taken into account in this plot.

two-dimensional  $\beta$ -model have shown that varying the center of the model, the core radii in two directions and  $\beta$  within reasonable limits one can change the amplitude of the longest perturbations (400-500 kpc) by a factor of two, compared to a symmetric  $\beta$ -model (see Fig.15). To illustrate this statement three models were used in Fig.15: (i) spherically symmetric  $\beta$ -model with  $\beta = 0.6$  and  $r_c = 9'$ ; (ii) two-dimensional  $\beta$ -model with  $\beta = 0.62$  and  $r_{c,x} = 9'$  and  $r_{c,y} = 8'$  and (iii) another two-dimensional model with  $\beta = 1.03$  and  $r_{c,x} = 15.9'$  and  $r_{c,y} = 13.5'$  (from Vikhlinin, Forman, & Jones 1994). The variations of the amplitude at large scales is not surprising, since with more complex models we are able to attribute some of the structures to the underlying model, rather than to perturbations. The amplitude of the perturbations at scales smaller than  $\sim 300$  kpc remains unchanged. In spite of the model-dependent variations of the amplitude at large scales, the structures seen in the images divided by the  $\beta$ -model are complicated enough, so it is probably fair to state that further reducing the amplitude of these structures would require substantially more complex models. We concluded that a conservative systematic uncertainty – a factor of order of 2 – should be attributed to large-scale perturbations, while at scales smaller than 300 kpc the systematic uncertainty is smaller.

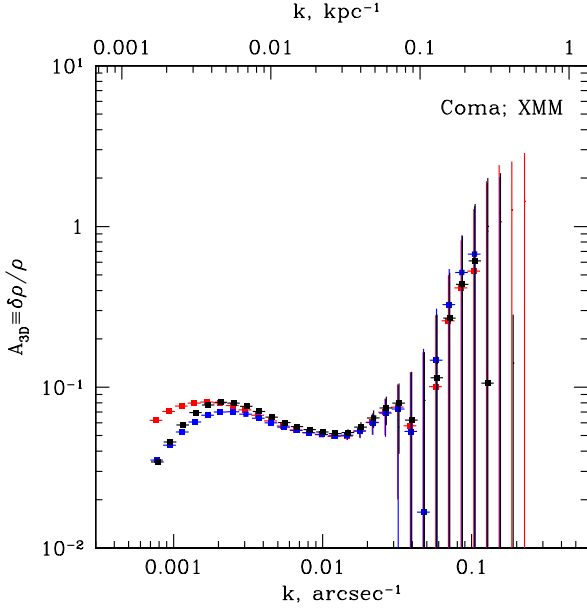


**Figure 15.** 3D amplitude of density fluctuations relative to different underlying  $\beta$ -models (based on XMM-Newton data). The red points (the same as shown in Fig.14) correspond to a spherically symmetric  $\beta$ -model with  $\beta = 0.6$  and  $r_c = 9'$ . The blue points correspond to a two-dimensional  $\beta$ -model with  $\beta = 0.62$  and  $r_{c,x} = 9'$  and  $r_{c,y} = 8'$ . The black points are for a model with  $\beta = 1.03$  and  $r_{c,x} = 15.9'$  and  $r_{c,y} = 13.5'$ . Depending on the parameters of the model the amplitude changes by a factor of 2 at scales above 500 kpc. At scales smaller than 300 kpc the power spectrum is virtually unchanged.

## 5.2 Perturbations of the gravitational potential

The gravitational potential of the cluster is affected by the presence of subhalos. In particular, in Coma there are two large cD galaxies – NGC 4874 and NGC 4889, with the X-ray surface brightness centroid lying in between these two objects. One can identify enhancements of the surface brightness at the positions of NGC 4874 and NGC 4889 (Vikhlinin, Forman, & Jones 1994), although the exact amplitude of these enhancements depends on the assumptions of the underlying cluster model<sup>5</sup>.

We can write the gravitational potential of the cluster as:

$$\varphi = \varphi_0 + \sum_i \Delta\varphi_i, \quad (23)$$

where  $\varphi_0$  is the smooth potential and  $\Delta\varphi_i$  is the perturbation, associated with the subhalo number  $i$ . To simplify the estimates we assume that for each of the two bright galaxies their potential can be written in an isothermal form over the

<sup>5</sup> Note that when calculating power spectra the  $15''$  circles around NGC 4874 and NGC 4889 have been excluded. Therefore the contributions of an AGN in NGC 4889 and cool coronae (Vikhlinin, Forman, & Jones 1994) in both galaxies are excluded.

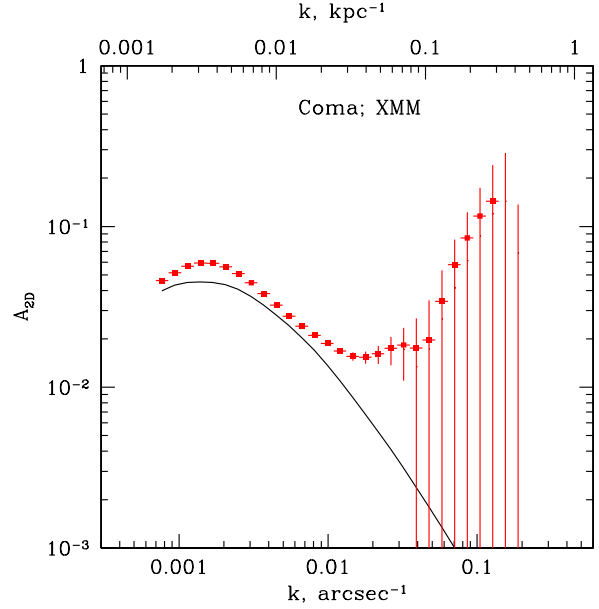


**Figure 16.** 2D relative amplitude of the surface brightness fluctuations (black line) caused by the presence of two components (representing gas concentration around two massive cD galaxies in Coma) on top of the global cluster emission. Parameters of the  $\beta$ -models for each galaxy and for the main cluster are taken from Vikhlinin, Forman, & Jones (1994). Note that the decomposition of the surface brightness into the three-component  $\beta$ -model is not unique. The same set of exclusion regions (around compact sources, including nuclei of NGC 4874 and NGC 4889) as for real data was used for the simulated dataset. For comparison, the 2D amplitude measured from XMM-Newton data is shown with red crosses.

interesting range of radii:

$$\Delta\varphi = v_c^2 \ln r + C, \quad (24)$$

where  $v_c$  is the circular speed and  $r$  is the galactocentric radius,  $C$  is an arbitrary additive constant. Further assuming that the gas is isothermal and ignoring possible effects of the galaxy motion with respect to the ICM, the relative gas density perturbation, induced by  $\Delta\varphi$  is taken out the first minus sign in the equation but perhaps you prefer the other way

$$\frac{\delta\rho}{\rho} = e^{\frac{-\mu m_p \Delta\varphi}{kT}} - 1 = \left(\frac{r}{r_s}\right)^{\frac{-\mu m_p v_c^2}{kT}} - 1, \quad (25)$$

where  $\mu \approx 0.61$  is the mean particle atomic weight,  $m_p$  is the proton mass,  $T$  is the ICM temperature,  $k$  is the Boltzmann constant and the overall normalization is expressed in terms of the scaling radius,  $r_s$  and the normalization constant  $C$  is chosen so that  $\Delta\varphi(r_s) = 0$ . For NGC 4874 and NGC 4889, Coccato, Gerhard, & Arnaboldi (2010) measured the line-of-sight velocity dispersion  $\sigma$  of  $\sim 283 \text{ km s}^{-1}$  and  $\sim 266 \text{ km s}^{-1}$  respectively at a distance of 50-60 kpc from their centers. For a spherical galaxy with

isotropic stellar orbits a reasonable estimate of the circular speed is then  $v_c \sim \sqrt{3}\sigma \sim 460 - 490 \text{ km s}^{-1}$ . Conservatively assuming  $v_c = 450 \text{ km/s}$  and the ICM temperature  $kT = 7 \text{ keV}$ , the resulting radial dependence of the density perturbation is  $\frac{\delta\rho}{\rho} \propto \left(\frac{r}{r_s}\right)^{-0.18} - 1$ . Further assuming that the perturbation of the potential extends up to  $r_s = 150 \text{ kpc}$  and is zero at larger distances, the RMS of the density variations induced by a single perturbation of the potential of this type can be estimated as follows:

$$\left(\frac{\int_0^{r_s} \left(\frac{\delta\rho}{\rho}\right)^2 4\pi r^2 dr}{\int_0^{r_{max}} 4\pi r^2 dr}\right)^{1/2} \approx 0.03, \quad (26)$$

where  $r_{max} \sim 325 \text{ kpc}$  is the characteristic size of the region which we analyze. To simplify this estimate we have assumed that the perturbation is located at the cluster center. This is a crude estimate, but it suggests that adding a single perturbation in a form of an isothermal halo with the above parameters is able to induce a volume averaged RMS of order 3%.

Another possibility to make this estimate is to fit the observed enhancements in the surface brightness around positions of the two bright galaxies and use the best fitting parameters to estimate the RMS. To this end we used a decomposition of the X-ray surface brightness into three  $\beta$ -models from Vikhlinin, Forman, & Jones (1994) - one for the main cluster and one for each of the two cD galaxies. Repeating the analysis for the three  $\beta$ -models image divided by the  $\beta$ -model for the cluster, we obtained a scale dependent relative amplitude of the surface brightness fluctuations induced by these galaxies (see Fig.16). For comparison we show the density fluctuations derived from the XMM-Newton image. Clearly, the amplitudes in the range of scales of order few 100 kpc are in the ballpark of values predicted by this simple exercise. This suggests that perturbations of the potential can be responsible for a significant part of the observed perturbations.

### 5.3 Turbulence

Turbulence is another possible source of pressure/density fluctuations in the ICM (e.g. Schuecker et al. 2004). Assuming an eddy with characteristic velocity  $v_{eddy}$  and adiabatic behavior of the gas one can relate the velocity and density perturbations as

$$\frac{\delta\rho}{\rho} \sim \frac{v_{eddy}^2}{2} \frac{1}{\gamma} \frac{\mu m_p}{kT} \sim M^2, \quad (27)$$

where  $\gamma = 5/3$  is the gas adiabatic index,  $\mu \sim 0.61$  is the particle mean atomic weight,  $m_p$  is the proton mass and  $M$  is the Mach number. For  $kT = 7 \text{ keV}$ , the value of  $v_{eddy} = 450 \text{ km s}^{-1}$  will induce 5.5% variations in the ICM density. Approximately (up to a factor of order unity) this corresponds to the ratio of the kinetic and thermal energies of the ICM. According to numerical simulations this is a perfectly reasonable value (e.g. Sunyaev, Norman, & Bryan 2003; Lau, Kravtsov, & Nagai 2009). It is not clear however

if numerical simulations can accurately predict the characteristics of the turbulent eddies (size and velocities), since the Reynolds numbers achieved so far are not very high (and we in fact do not know the effective viscosity of the ICM).

The assumption that a significant part of the observed fluctuations is due to perturbations of the gravitational potential (see §5.2) would imply that the level of turbulence is modest. For instance one can use Fig.16 to estimate the amplitude of fluctuations on top of the contribution induced by gas concentration around the two massive cD galaxies. These excess fluctuations of density have an amplitude of order 2-4% on scales  $\sim 30-300 \text{ kpc}$ , which corresponds to a velocity amplitude of  $\sim 300-400 \text{ km s}^{-1}$  according to eq.27. This in turn implies that the contribution of turbulent pressure support is similarly low. Accounting for the gas entropy fluctuations considered in section §5.5 may lower this estimate even further. Of course accurate estimates of the turbulent pressure support by this method are difficult. Future observations with X-ray micro-calorimeters, initially from ASTRO-H (e.g. Takahashi et al. 2010), should be able to constrain both the velocities and sizes of the energy-containing eddies (e.g. Zhuravleva et al. 2011). For now, turbulence remains a plausible contributor to the observed surface brightness fluctuations, as well as pressure fluctuations (Schuecker et al. 2004) in Coma.

### 5.4 Sound waves generated by the turbulence

It is interesting to estimate a possible contribution of sound waves to the observed surface brightness variations. The advantage of sound waves is that they represent a linear relation (rather than quadratic) between the gas velocity and the pressure/density perturbation:

$$\frac{\delta\rho}{\rho} \sim \frac{v}{c_s}, \quad (28)$$

where  $c_s$  is the sound speed. E.g. to produce 5% variations in density one needs  $v \sim 70 \text{ km s}^{-1}$ . Sound waves cross the region of interest  $R \sim 350 \text{ kpc}$  over  $t_s = R/c_s$ . If one assumes that the sound waves are generated by the turbulence, then the rate of sound-wave generation per unit volume ( $\text{ergs s}^{-1} \text{ cm}^{-3}$ ) is (Lighthill 1952; Landau & Lifshitz 1987, §75)

$$\dot{\epsilon} \propto \frac{v_{eddy}^8}{c_s^5 l}, \quad (29)$$

where  $l$  is the characteristic eddy size. The typical amplitude of the gas velocity due to sound waves in the region of size  $R$  (assuming that turbulence generates sound waves uniformly over the region with volume  $\sim R^3$ ) can be estimated as

$$v \approx \sqrt{\dot{\epsilon} t_s} = v_{eddy} \left(\frac{v_{eddy}}{c_s}\right)^3 \sqrt{\frac{R}{l}} \sim 30 \text{ km s}^{-1}, \quad (30)$$

where we assumed  $v_{eddy} = 450 \text{ km s}^{-1}$  and  $l = 100 \text{ kpc}$ . Thus sound waves generated by turbulence, are not very effective in producing density perturbations unless the turbulent velocities generating the sound waves are larger than  $450 \text{ km s}^{-1}$ . Of course the above argument provides only an order of magnitude estimate.

### 5.5 Entropy variations

Another natural mechanism, which may cause density variations is the variation of entropy/temperature. We distinguish them from potential perturbations, turbulent pulsations or sound waves, since entropy variations can exist without associated strong pressure perturbations (to lowest order in Mach number). We assume that in these perturbations

$$\frac{\delta\rho}{\rho} \sim -\frac{\delta T}{T}, \quad (31)$$

where  $T$  is the gas temperature.

One can identify two different modes of entropy perturbations. The first mode is associated with the low entropy gas, infalling into the system. One of the features, seen in the Coma images, namely a chain of galaxies apparently infalling into Coma from the East (Vikhlinin, Forman, & Jones 1997) is associated with colder gas, which is clearly seen in the hardness ratio map (e.g. Neumann et al. 2003). In Fig.12 this cold stream appears as an enhancement in the surface brightness relative to the cluster  $\beta$ -model. The amplitude and the area covered by this feature are comparable with the perturbations, identified as a potential perturbation in §5.2. We therefore can expect a similar impact of this feature on the final estimate of the density perturbations.

Another possibility to create entropy fluctuations is the advection of gas with different entropies by gas motions in turbulent eddies. Assuming an unperturbed isothermal atmosphere of the cluster with density following a  $\beta$ -model, we can estimate the eddy size needed to create the required density contrast. When a gas lump is advected from the radius  $r$ , where the gas pressure is  $P$ , to the radius  $r + \delta r$ , where the pressure is  $P - \delta P$ , and it expands adiabatically, the corresponding density change is

$$\frac{\delta\rho}{\rho} = \frac{1}{\gamma} \frac{\delta P}{P} \approx -\frac{1}{\gamma} 3\beta \left(\frac{\delta r}{r}\right) \frac{\left(\frac{r}{r_c}\right)^2}{1 + \left(\frac{r}{r_c}\right)^2}. \quad (32)$$

Near the core radius  $r \approx r_c$  a 10% change in radius causes a  $\sim 5\%$  change of density. Thus eddies of size  $\delta r \sim 0.1r_c \sim 25-30$  kpc are needed. As in the case of turbulent fluctuations, future measurements of eddy amplitudes and sizes would provide crucial constraints on the contribution of this mode.

### 5.6 Metallicity variations

In the 0.6-2.5 keV band the change of metallicity from 0.5 solar to 1 solar (for  $kT = 8$  keV APEC model, Smith et al. (2001)) causes a 5.6% increase in the count rate (for XMM-Newton). The change of density, causing the same increase of the flux is  $5.6/2=2.8\%$ . Thus very strong variations of metallicity are needed if they are to make a significant contribution to variations of emissivity.

### 5.7 Bubbles of relativistic plasma

Observations of cool-core clusters revealed rich substructure caused by the presence of AGN-inflated bubbles of relativistic plasma (e.g. Churazov et al. 2000). In terms of X-ray

surface brightness perturbations, the bubbles reveal themselves as depressions in the surface brightness with the amplitude set by the fraction of the line-of-sight volume occupied by the bubbles. In cool-core clusters, the fraction of the volume occupied by bubbles can be large - of order 10% or more. The RMS variations of the density perturbations will be high accordingly. In Coma there is no compelling evidence for widespread bubbles of relativistic plasma, although one of the cD galaxies - NGC4874 does contain an active radio source with a pair of bubbles on each side of the nucleus (Sun et al. 2005). Future low frequency radio observations might reveal radio bright regions (associated with low energy electrons contained in bubbles). If these regions correlate with the X-ray surface brightness depressions, this would be a key indicator in favor of this mechanism. For now we can only state that in Coma, radio bubbles are a possible source of X-ray surface brightness fluctuations, although there exists no compelling evidence that this mechanism is really important for Coma.

## 6 CONCLUSIONS

X-ray surface brightness fluctuations in the core ( $650 \times 650$  kpc) region of the Coma cluster are analyzed using XMM-Newton and Chandra images and converted into scale-dependent amplitudes of volume-filling ICM density perturbations. The characteristic amplitudes relative to a smooth underlying density are modest: they vary from 7-10% on scales of 500 kpc down to  $\sim 5\%$  at scales  $\sim 30$  kpc<sup>6</sup>. At smaller scales, projection effects and the PSF (for XMM-Newton) smear the density fluctuations by a large factor, precluding strong limits on the density fluctuations in 3D. Nevertheless making deep ( $\sim$  Msec long) Chandra exposures can still be useful in pushing down the constraints for scales smaller than 30 kpc.

Several physical effects can contribute to observed fluctuations of the surface brightness/density. The most likely contributors at large scales are the perturbations of the gravitational potential by massive cD galaxies and entropy variations due to infalling cold gas. We do see in raw images the substructure which can be plausibly associated with these mechanisms.

Other effects can contribute to the observed fluctuations, including variations of density in turbulent eddies, advection of the low/high entropy gas by turbulent eddies, generation of sound waves by turbulence, bubbles of relativistic plasma and metallicity variations. Future high energy resolution X-ray missions (e.g. ASTRO-H) and low frequency radio observations (e.g. LOFAR) could help differentiate between these possibilities. At present we can consider the detected variations as conservative limits on the amplitude of the density/emissivity fluctuations caused by any of these effects.

Despite a variety of possible origins for density fluctuations, the gas in the Coma cluster core is remarkably ho-

<sup>6</sup> for comparison the mean free path for Coulomb collisions in the core of Coma is of order 5 kpc

mogeneous on scales from  $\sim 500$  to  $\sim 30$  kpc, with density variations relative to a plausible smooth model smaller than 10%.

## 7 ACKNOWLEDGMENTS

This research has made use of data obtained from the Chandra and XMM-Newton Archives. This work was supported in part by the Leverhulme Trust Network for Magnetized Plasma Turbulence and STFC Grant ST/F002505/2 (AAS). The work was supported in part by the Division of Physical Sciences of the RAS (the program “Extended objects in the Universe”, OFN-16). The financial support for SWR was partially provided for by the Chandra X-ray Center through NASA contract NAS8- 03060, and the Smithsonian Institution.

## REFERENCES

- Anders E., Grevesse N. 1989, *Geochim. Cosmochim. Acta*, 53, 197
- Arévalo P., Churazov E., Zhuravleva I., Hernández-Monteagudo C., Revnivtsev M., 2011, *ApJ*, submitted
- Cavaliere A., Fusco-Femiano R., 1978, *A&A*, 70, 677
- Churazov E., Forman W., Jones C., Böhringer H., 2000, *A&A*, 356, 788
- Coccatto L., Gerhard O., Arnaboldi M., 2010, *MNRAS*, 407, L26
- Kawahara H., Reese E. D., Kitayama T., Sasaki S., Suto Y., 2008, *ApJ*, 687, 936
- Landau L. D., Lifshitz E. M., 1987, *Fluid Mechanics*, Pergamon Press.
- Lau E. T., Kravtsov A. V., Nagai D., 2009, *ApJ*, 705, 1129
- Lighthill M. J., 1952, *RSPSA*, 211, 564
- Neumann D. M., Lumb D. H., Pratt G. W., Briel U. G., 2003, *A&A*, 400, 811
- Ossenkopf V., Krips M., Stutzki J., 2008, *A&A*, 485, 917
- Peacock J. A., 1999, *Cosmological physics*, Cambridge University Press
- Schuecker P., Finoguenov A., Miniati F., Böhringer H., Briel U. G., 2004, *A&A*, 426, 387
- Smith R. K., Brickhouse N. S., Liedahl D. A., Raymond J. C., 2001, *ApJ*, 556, L91
- Soltan A., Fabricant D. G., 1990, *ApJ*, 364, 433
- Sun M., Vikhlinin A., Forman W., Jones C., Murray S. S., 2005, *ApJ*, 619, 169
- Sunyaev R. A., Norman M. L., Bryan G. L., 2003, *AstL*, 29, 783
- Takahashi T., et al., 2010, *SPIE*, 7732,
- Vikhlinin A., Forman W., Jones C., 1994, *ApJ*, 435, 162
- Vikhlinin A., Forman W., Jones C., 1997, *ApJ*, 474, L7
- Vikhlinin A., Markevitch M., Murray S. S., Jones C., Forman W., Van Speybroeck L., 2005, *ApJ*, 628, 655
- Zhuravleva I., Churazov E., Kravtsov A., Sunyaev R., 2012, *MNRAS*, submitted